J Mater Sci (2011) 46:385–393
DOI 10.1007/s10853-010-4848-y

Mechanical properties and deformation mechanisms of nanocrystalline Fe/Cu 60/40 composites

V. L. Tagarielli · N. A. Fleck · A. Colella · P. Matteazzi

Received: 8 September 2009 / Accepted: 9 November 2009 / Published online: 8 September 2010

Abstract The effect of grain size upon the strength of nanocrystalline iron/copper (Fe/Cu) composites has been explored. Composites of composition 60 Fe/40 Cu (by weight) were produced by consolidation of ball-milled powders, with as-processed grain size ranging from 80 to 150 nm. All composites displayed negligible strain hardening and a symmetric response in tension and compression. The strength increases with diminishing grain size, and the upper and lower yield points are a consequence of the dissolved carbon in the Fe phase. The nanocrystalline composites develop shear bands in both tension and compression, and the geometric evolution of these bands is determined. The width of each band and the average local shear strain within it increases with increasing global plastic strain. AFM measurements reveal that the shear strain within each band has strong spatial gradients.

Introduction

Nanocrystalline metallic alloys show potential for engineering application due to their high strength, but the mechanisms which govern their deformation and failure are not completely understood, see, for example, the reviews by Meyer et al. [1] and Suryanarayana et al. [2] for a collection of recent experimental and modelling work. A number of processing techniques have been developed to produce nanocrystalline materials, but these are often limited to small volume components [3] or thin films. In this study, we shall examine the mechanical properties of bulk samples of iron–copper alloys produced by the ball milling of nanocrystalline powders and subsequent powder consolidation and heat treatment.

It is commonly observed that a decrease in grain size of nanocrystalline metal leads to an increase in strength and hardness, and to a decrease in tensile ductility, consistent with a drop in strain hardening rate, see, for example, [4], [5]. Akhtar et al. [6] have investigated the compressive response of nanocrystalline copper produced from ball-milled powder, with grains ranging from 22 to 720 nm. They observed that the yield stress and the strain rate sensitivity increased, while the strain hardening rate decreased, with diminishing grain size. Zhang et al. [7] have examined the response of nano- and microcrystalline Zn as a function of grain size, and have shown that the hardness increases and the ductility decreases with decreasing grain size. Optimal combinations of strength and ductility were achieved by the manufacture of "hybrid" microstructures containing larger grains (>50 nm) within a nanocrystalline matrix.

Nanocrystalline metals are often manufactured as composites, comprising two or more distinct metallic phases. This has the double objective of combining the properties of the constituent materials, and hampering grain growth during high temperature consolidation. Iron/Copper (Fe/Cu) composites, designed with a view to combine the strength and stiffness of Fe with the high thermal and electrical conductivities of Cu, have been studied by

V. L. Tagarielli · N. A. Fleck (✉)
Department of Engineering, Cambridge University,
Trumpington St., Cambridge CB2 1PZ, UK
e-mail: naf1@eng.cam.ac.uk

A. Colella
CSGI Via della Lastruccia, 50019 Sesto Fiorentino, Italy

P. Matteazzi
MBN Nanomaterialia S.p.A, Via Bortolan 42-A,
31050 Vascon di Carbonera, Italy
e-mail: info@mbn.it
URL: www.mbn.it

several authors [8]. Nanocrystalline Fe/Cu material systems are examined in this study; earlier studies on this material system revealed that high hardness and strength can be achieved by reducing the grain size of both constituents ([9], [10]). Some authors (see, e.g., Aifantis and co-workers [11]) have reported a pronounced tension–compression asymmetry in strength, and have observed the formation of shear bands, for Fe/Cu 90/10 systems with grain sizes ranging from 45 to 1700 nm.

In this study, we consider the mechanical response of three Fe/Cu 60/40 systems, manufactured by powder consolidation, having grain sizes ranging from 80 to 150 nm. In the "Materials and processing" section, we describe the materials employed and, in the "Measurements" section, we give details of the tests performed. In the "Conclusions" section, the experimental observations are reported and discussed. Some attention will be paid to the strain distribution that develops within shear bands in selected compression tests.

Materials and processing

Three nanocrystalline metallic iron–copper composites were manufactured and tested. Each composite was prepared by the consolidation of powders produced by mechanical alloying at MBN Nanomaterialia. Iron and copper powders were mixed (60 and 40% by weight, respectively) and were processed for 6–12 h in a ball-milling machine with stainless steel balls. The process involved repeated impact of the powder particles by the steel balls and consequent fracturing and welding, resulting in a fine-grained final structure of the powder. Before ball milling, the powder particles were of diameter approximately 0.5 μm. After 6 h of ball milling, the sizes of the iron (Fe) and copper (Cu) grains were 18 and 17 nm, respectively, as determined by X-ray diffraction analysis of the powders. Longer ball-milling times (12 h) produced average grain sizes of 14 and 13 nm for the Fe and Cu, respectively.

The powders were then consolidated by hot extrusion. Three different consolidation routes were followed, resulting in different crystalline structures of the consolidated materials. The high temperature exposure during the extrusion process resulted in grain growth; this growth was somewhat impeded by the biphasic nature of the metallic composite, which comprised two fine inter-penetrating networks of iron and copper, as will be shown below.

Material A: nanocrystalline Fe/Cu 60/40, extruded and HIPed

Ball-milled powder (processed for 6 h) was placed in a vacuum bag and was inserted in an induction-heated, metallic extrusion die. A vacuum was enforced to prevent oxidation, and the system was brought to a temperature of 1173 K and extruded using an extrusion ratio of 15:1. The extruded material was then subjected to hot hydrostatic pressing (HIP) in an argon atmosphere at a temperature of 973 K and a pressure of 100 MPa for 30 min. Subsequently, the HIPed material was cooled to 673 K over 30 min and was finally cooled to room temperature.

A chemical analysis revealed that carbon was present in weight concentration 0.2%, with trace concentrations of oxygen at 1300 ppm and nitrogen at 100 ppm. Preliminary analysis by X-ray diffraction and the Sherrer's formula suggested average grain sizes of 127 and 119 nm for the iron and copper grains, respectively.

Material B: nanocrystalline Fe/Cu 60/40, extruded

This material was obtained via an identical route as for *material A*, absent the HIPing process. The ball-milled powders where placed in a vacuum bag and extruded at a temperature of 1173 K with an extrusion ratio of 15:1. The chemical composition was the same as for *material A*; on the other hand, the absence of the HIPing process for *material B* resulted in smaller grain size; X-ray diffraction revealed average grain sizes of 89 and 90 nm for the iron and copper grains, respectively.

Material C: nanocrystalline Fe/Cu 60/40, double-extruded

In order to obtain a finer crystalline microstructure, the powders utilised for this material were processed in the ball-milling machine for 12 h; subsequently, they were consolidated by two consecutive extrusion processes, each using an extrusion ratio of 4:1. The first extrusion was performed at a temperature of 743 K and the second at 873 K. The reduced extrusion temperature compared to that for material *B* delayed grain growth, as shown by X-ray diffraction analysis: the average grain sizes of the iron and copper phases were 86 and 80 nm, respectively.

Measurements

Characterisation of the microstructure

The densities of the as-consolidated materials were 8210, 8180 and 8130 kg m^{-3} for materials *A*, *B* and *C*, respectively. Note that these measured densities are slightly less than the value of 8230 kg m^{-3}, as calculated by the rule-of-mixtures formula for a Fe/Cu 60/40% composite. This is due to the nanocrystalline nature of the materials under investigation, in which grain boundaries (of reduced density) represent a considerable volume fraction of the material.

Optical, electronic and atomic force microscope observations were used to analyse the microstructure of the three composites. First, samples of each composite were mounted in an acrylic resin and mechanically polished to a roughness of 50 nm, and were then observed in an optical microscope. Defects were present in the form of Fe-rich or Cu-rich zones; these zones typically extended along the extrusion direction and were approximately 50 μm in length, and 5 μm in width. For materials *B* and *C*, which did not undergo HIPing, occasional pores were also observed.

In order to obtain additional microstructural details, the nanocrystalline composites were mechanically polished and examined in a field emission scanning electron microscope (FESEM). Before examination, a focused ion beam (FIB) was used to remove a wedge of material as sketched in Fig. 1a, exposing a flat and vertical surface. This surface was then observed via FESEM, using a back-scatter electron detector, as shown in Fig. 1b. This technique revealed two interpenetrating networks of Fe and Cu phases, for all the three materials.

A representative FESEM picture is shown in Fig. 1b for *material B*. Darker regions indicate Cu, whereas brighter regions represent Fe (the back-scatter electron detector provides contrast for different atomic numbers). The width of the Fe or Cu phases was approximately 1–2 μm, and no preferential orientation of these phases was observed. In each Fe or Cu phase, a polycrystalline structure was detected, but this was not clearly visible in the FESEM, due to the small grain size and to the magnetic nature of the material. The grain size was estimated from the X-ray analysis using Sherrer's formula, although it is recognised that the accuracy of this formula is limited to grains of size below 50 nm. In order to obtain a more accurate measurement of the average grain size for each of the three nanocrystalline composites, an atomic force microscope (AFM) was also used.

The AFM was operated in both contact mode (to measure surface topology and locate suitably flat areas of observation) and non-contact mode (to obtain more detailed measurements of the grain size). In the non-contact mode, the phase signal was recorded to distinguish Fe from Cu regions, while the amplitude signal was employed to reveal the topology of the small Fe or Cu grains. Figure 1c shows an example of the amplitude signal distribution over an area of 600 × 600 nm, for the case of a Cu region in *material B*. Grains are visible, of average size 100 nm. The FESEM and AFM analyses were performed on the three composite materials, and the measured grain sizes for each composite are tabulated in Table 1, along with the mechanical properties measured in this study. Note that the grain size as measured by the AFM was comparable to that predicted by Sherrer's formula.

Uniaxial tests

Quasi-static experiments were carried out to determine the uniaxial tensile and compressive responses of the nanocrystalline composites. Compression tests were performed on circular cylinders of diameter 3 mm and height 6 mm. The cylinders were cut from the extruded material using a wire spark-erosion machine; a lathe was then used to

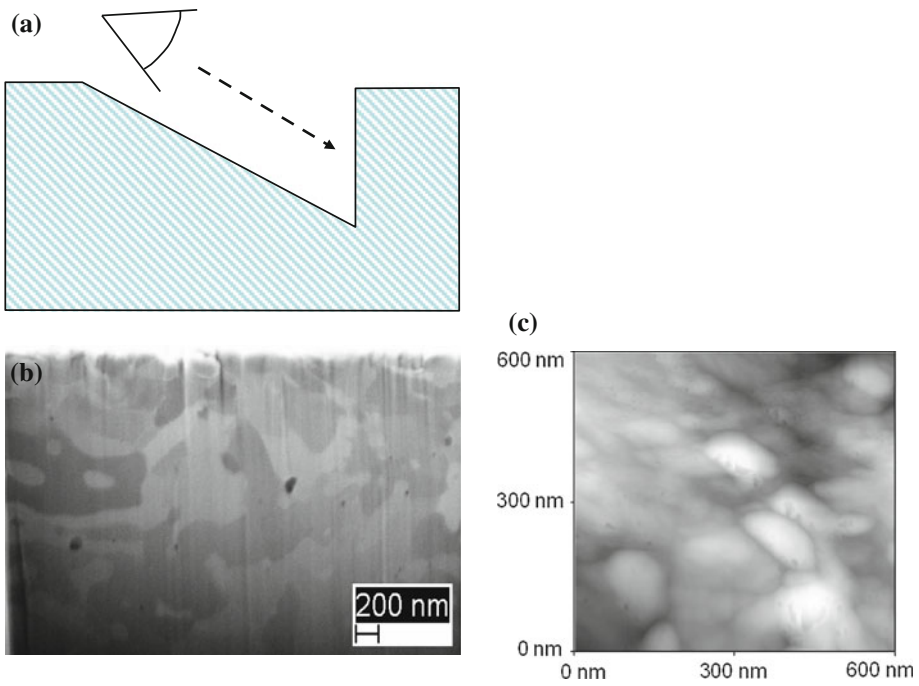

Fig. 1 Microstructure of *material B*. **a** Schematics of the FIB milling. **b** FESEM picture of a FIB machined area—a back-scatter electron detector was used. **c** AFM image of a Cu region, amplitude signal in non-contact mode

Table 1 Composition, grain size and mechanical properties of the three nanocrystalline materials tested in this study

Material	Grain size nm (Sherrer)		Grain size nm (AFM)	ρ (kg m^3)	E (Gpa)	σ_{peak} (MPa)	ε_f (%)	HV_{300}
	Fe	Cu						
A	127	119	150	8210	188	747	10	192
B	89	90	100	8180	180	860	12	224
C	86	80	80	8130	178	1245	1	335

face-off the ends and to mechanically polish their lateral surfaces by a 4000-grit polishing paper.

A screw-driven testing machine was used to load the cylindrical specimens axially via two hardened steel plates, lubricated with a PTFE spray. The load was recorded by the load cell of the testing machine, while the relative displacement of the loading steel plates was monitored via a laser extensometer. In some tests, a miniaturised resistance strain gauge was also adhered to the lateral surface of the specimen to obtain a more accurate strain measurement. The approach velocity of the loading plates was chosen to give an imposed nominal strain rate of 10^{-3} s^{-1} in all tests.

The compressive responses of materials *A*, *B* and *C* are compared in Fig. 2a, in the form of true stress versus true (logarithmic) compressive strain. Salient values are summarised in Table 1. Materials *A* and *B* display similar behaviours: a linear elastic response, followed by plastic deformation at stress levels of approximately 500 and 600 MPa, for *materials A* and *B*, respectively. The elasto-plastic stress/strain response displays a peak in stress at true strains on the order of 0.5%. The stress level then drops by about 100 MPa, and negligible strain hardening accompanies the ensuing response up to a large nominal compressive strain of approximately 60%, at which point the tests were terminated.

The behaviours of materials *A* and *B* were similar in shape but the *material B*, of smaller grain size, displayed a slightly stronger response. The compressive response of *material C* was qualitatively different; an elastic response is followed by the initiation of plasticity at a true stress of approximately 750 MPa, with subsequent strain hardening and brittle failure. The fracture event occurred at the peak stress of 1250 MPa, and involved the unstable propagation of a planar crack oriented at 45° with respect to the axis of the cylinder.

Uniaxial tension tests were performed as follows. Axi-symmetric specimens of circular cross section and dog-bone profile were machined in a lathe starting from 3 mm diameter, 50 mm long circular bars. The final dog-bone-shaped sample resembled fatigue specimens, with a uniform diameter in the gauge length and threaded ends of larger diameter. The uniform portion of the specimen had a diameter of 1.7 mm and length of 5 mm, and was mechanically polished in a lathe with 4000-grit polishing paper; both ends of the sample were given M2.5 metric threads.

The threaded ends of the sample were fastened to a hardened steel rig, attached to the testing machine, and the displacement rate of the cross-head of the screw-driven machine was chosen to give an imposed nominal strain rate of 10^{-3} s^{-1} on the sample. The load was again recorded by the load cell of the testing machine. Miniaturised resistance strain gauges, of gauge length 0.3 mm, were adhered on two opposite sides of the specimen to measure the uniform strains in the gauge section, and were connected to a Wheatstone bridge and a low-noise amplifier. Additional strain measurements were conducted via a laser extensometer.

The measured tensile responses are included in Fig. 2a. The strain gauges were employed to determine the Young's modulus of the composites: the measured value was approximately 180 GPa and was scarcely sensitive to grain size (see Table 1). For materials *A* and *B*, the tensile response was similar to that in compression: both upper

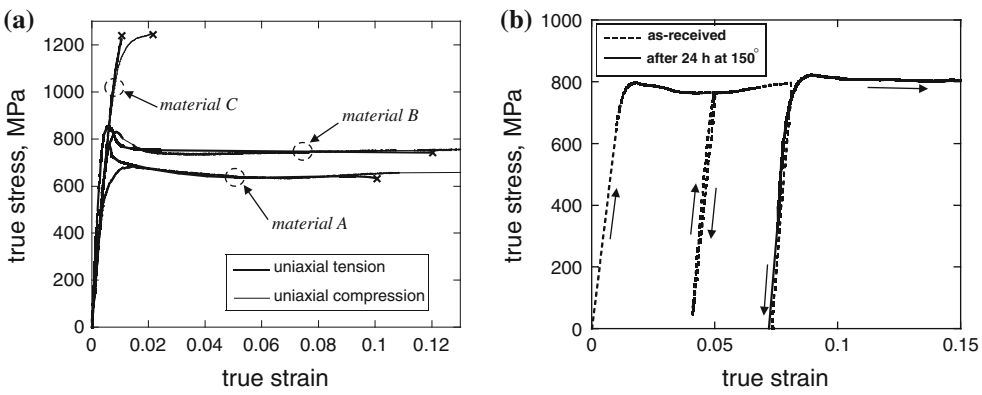

Fig. 2 **a** Uniaxial tensile and compressive stress versus strain responses for the nanocrystalline materials tested in this study. **b** Ageing experiment: the uniaxial compressive stress versus strain response of *material B* before and after the ageing cycle

and lower yield points were detected. The low subsequent hardening rate led to a 'cup and cone' instability at a axial strains of 10 and 12%, for materials A and B, respectively. A ductile fracture mechanism occurred with microvoid coalescence occurring in both the central cup and in the adjoining shear lips.

The tensile response of *material C* was different to its compressive behaviour, see Fig. 2a. In tension, material *C* exhibited a linear elastic response up to a stress of 750 MPa followed by an elasto-plastic response with strong strain hardening. At a stress of 1250 MPa, and a tensile strain of 1%, the specimen fractured. A negligible degree of necking was evident; however, the two ends of the fractured specimen again possessed the 'cup and cone' shape; in the central part of the fractured surface, microvoid coalescences were observed by SEM examination, with voids of approximate diameter 0.5 μm.

From the experiments described above, and as reported in Fig. 2a, it was concluded that the response of the nanocrystalline composites was symmetrical in tension and compression, with comparable failure stresses in these two loading cases; this is in contrast with the observations by Aifantis and coworkers [11], but we note that those authors had examined Fe/Cu 90/10 systems. The ductilities of materials *A* and *B* were of the order of 10%, whereas for *material C*, of smaller grain size, the ductility was only of order 1%. *Material C* fractured in compression as well as in tension, in contrast with the response of materials *A* and *B*, which fractured in tension but displayed a large ductility in compression.

Ageing experiments

As noted above, both the tensile and compressive stress/strain responses of *materials A* and *B* display upper and lower yield points (*Material C* does not display this peak due to premature failure in both tension and compression.). The occurrence of an 'upper' and a 'lower' yield point in ferritic structural steels is due to dislocation pinning by carbon or nitrogen [12]. After unpinning, the dislocations move more freely in the crystal, resulting in reduced flow strength.

In order to confirm that the observed peak stress in the nanocrystalline Fe/Cu composites arises from interstitial atoms pinning dislocations, a series of ageing experiments were performed as follows. First, compression experiments were carried out on circular cylindrical specimens (see Fig. 2b for the response of *material B*). The stress/strain response displayed the peak in stress, followed by a plateau. During unloading, the material response was linear elastic and upon reloading, the stress/strain curve did not display the peak in stress, consistent with the notion that the unpinned dislocations remained free to glide.

Subsequently, the deformed specimens were placed in an air furnace at a temperature of 150 °C for 24 h, and the compression tests were repeated. After this ageing treatment, the upper yield point was re-established, as shown in Fig. 2b. We explain this strain-ageing phenomenon by noting that 0.2% of C was present, and interstitial C atoms acted as the pinning points for dislocations. The thermal ageing treatment allowed the C atoms to diffuse in the crystal and re-pin the dislocations.

Cyclic plastic straining

The response of *materials A* and *B* to cyclic plastic straining in tension/compression was also measured, to determine whether a Bauschinger effect was present. For *material C,* this measurement could not be performed due to its very low tensile ductility. If yielding is associated with the pile-up of dislocations with attendant back-stresses, then a Bauschinger effect is anticipated. Conversely, if bulk plastic flow is more dissipative than energetic in nature (see the discussion in Fleck and Willis [13]), then a negligible Bauschinger effect will exist.

Axisymmetric dog-bone-shaped specimens were prepared, identical to those employed for the tensile tests described above. Resistance strain gauges were adhered to the specimens, and the load was recorded by the load cell of the screw-driven testing machine; tests were performed in displacement control.

Figure 3 reports the uniaxial tension/compression response of *material B* (*material A* shows the same features, and the results are not reported here for the sake of brevity). The sample was initially loaded in compression, and the material displayed both upper and lower yield points, followed by a stress-plateau. The loading direction was reversed at a true compressive strain of approximately 3%, and the material was then deformed up to a tensile strain of 3%. An additional straining cycle was performed, with limit strains of $\pm 1.5\%$.

The value of the flow stress for *material B* is indicated in Fig. 3 at selected points on the stress/strain response. A cyclic softening behaviour is also observed, with the plastic flow stress decreasing with each load reversal. No Bauschinger effect is noted: had only a single reversed loading cycle been performed, we would have incorrectly concluded that a Bauschinger effect is present. We conclude that grain boundary strengthening is progressively diminished with cyclic loading.

Instrumented nanoindentation

In order to probe the strength of the individual Fe and Cu phases, a series of nanoindentation experiments were performed. As noted above, the Fe and Cu phases are finely

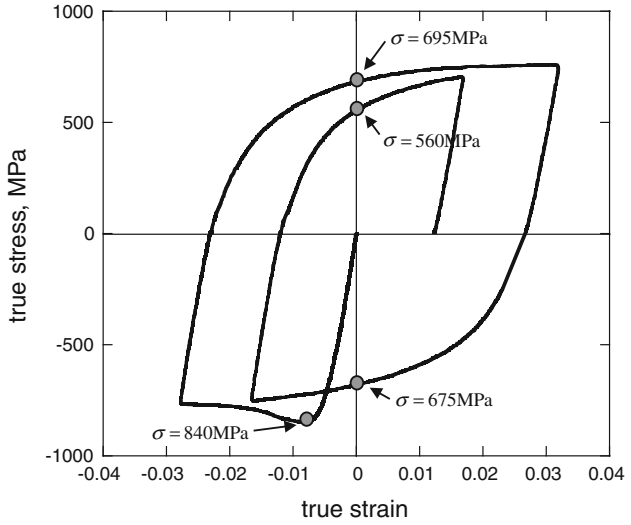

Fig. 3 Uniaxial stress versus strain response of *material B* to cyclic tension–compression plastic straining

mixed in the composites, and the typical width of the Fe or Cu phases is on the order of 1 μm. Indents of width 260 nm were applied to probe the hardness of each phase, and a FESEM was used to determine the location of the indents with respect to the underlying microstructure. The details are as follows.

A disc of *material B* was machined to a diameter of 3 mm and a thickness of 2 mm, and was then mounted in acrylic resin and mechanically polished to a roughness of 50 nm. A FIB was used to remove a surface layer (approximately 5 μm deep) from the specimen, over an area of 100 μm × 100 μm exposing a flat and smooth surface for the indentation tests.

An instrumented nanoindenter with a three-sided Berkovich pyramidal tip was used to perform a series of indentation tests. The indentations formed a 5 × 5 square grid with a spacing of 5 μm, and the indenter was subjected to a maximum penetration depth of 50 nm. The loads versus displacement traces were measured, and the hardness was determined for each indentation; two examples of load/displacement response are shown in Fig. 4a for two selected experiments for which the indenter's footprint fell entirely within a Fe or a Cu region; these measurements show that the Fe phase is harder than the Cu phase.

After the tests, the specimen was observed in a FESEM. A secondary electron detector was used to reveal the surface topology: the triangular impressions had negligible material pile-up or sink-in. A back-scatter electron detector was employed to determine which phases (Fe or Cu, or both) were spanned by the indenter footprint.

Figure 4b presents measured nanohardness data, plotted as a function of the percentage of Fe phase spanned by the indenter footprint. The hardness increases with the percentage of Fe under the indenter. The lowest measured values of hardness are for indenter footprints spanning Cu only, whereas the highest values are for indentation fully within the Fe regions; the ratio of hardnesses is about 2.

Observation of shear bands in uniaxial tests

Shear bands were observed on the surface of the specimens subjected to tensile or compressive loading. In order to explore the evolution of these bands with macroscopic strain, an interrupted compression test was performed on a sample of *material B*, as follows.

Observation of shear bands

A circular cylinder of diameter 3 mm and length 6 mm was mechanically polished down to a roughness of 50 nm on its lateral surface to generate two flat and perpendicular faces, as sketched in Fig. 5a. The specimen was loaded in axial compression at a nominal strain rate of 10^{-3} s^{-1}, and the test was interrupted when a plastic strain of 0.4% was attained. Shear bands of orientation close to 45° with respect to the axis of the specimen were detected, as shown in Fig. 5b. The width of the shear bands ranged from a few microns to nearly 100 μm.

Subsequently, the specimen was compressed further to a compressive plastic strain of 0.8%. Figure 5b compares the

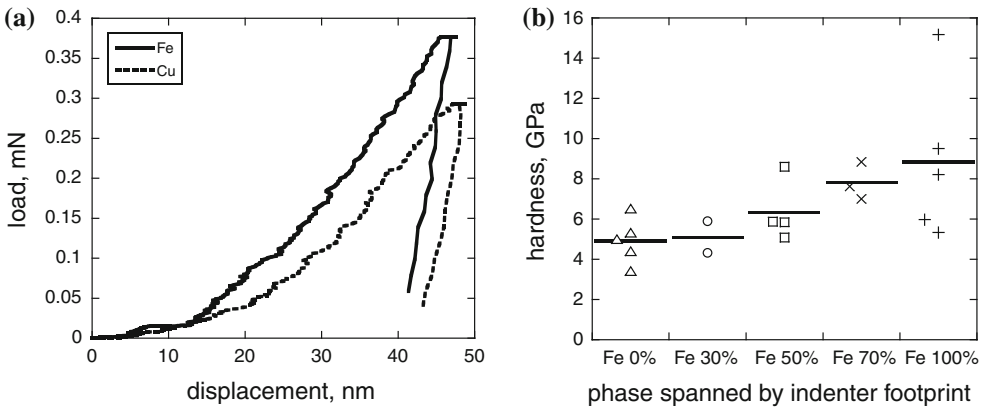

Fig. 4 **a** Load versus displacement response for the nanoindentation of *material B*. Two curves are compared, corresponding to indentations for which the indenter footprint falls entirely within either the Fe or Cu phases. **b** Measured nanohardness versus percentage of Fe phase spanned by the footprint of the Berkovich indenter

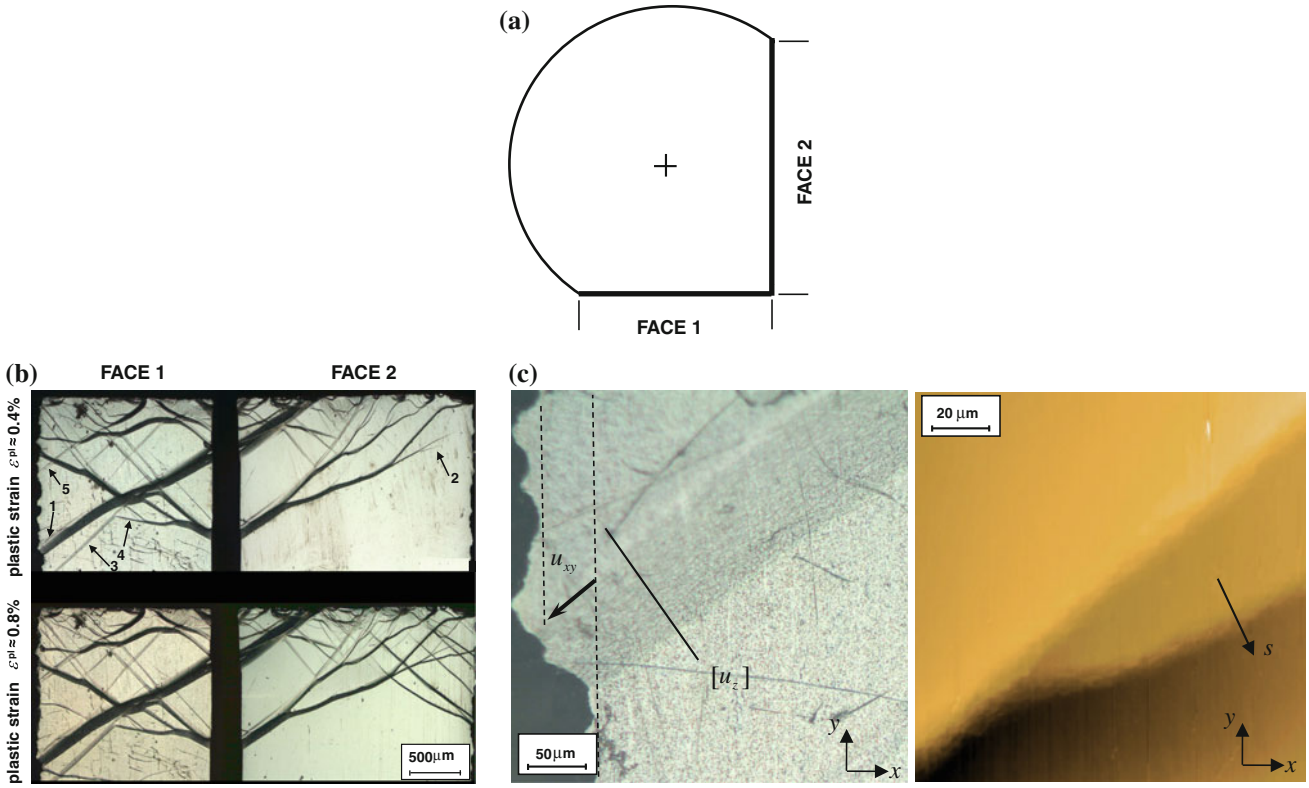

Fig. 5 **a** Cross section of the cylindrical compression specimen employed to visualize shear bands within the nanocrystalline *material B*. **b** Shear bands developing on the two flat faces of the specimen, and their evolution with the overall applied plastic strain. **c** Measurements on the shear bands; on the *left-hand side*, an optical picture of band 1; on the *right-hand side*, an AFM image of band 2; both images are taken at a plastic strain of 0.4%

patterns of shear bands obtained after compressive plastic straining of 0.4 and 0.8%. Numbered arrows in the upper part of the figure indicate shear bands that widen as the strain is incremented from 0.4 to 0.8%. Most of these bands increase their width as the overall plastic strain on the specimen increases; some bands, such as that indicated by the number 2, also lengthen in a crack-like manner.

In order to determine the average shear strain within two selected shear bands (namely, bands 1 and 2), the relative displacement of the material blocks adjacent to each of these two bands was measured, at compressive plastic strains of 0.4 and 0.8%. This relative displacement is in general the vector sum of an in-plane component u_{xy} and an out-of-plane component u_z.

For band 1, the out-of-plane relative displacement jump $[u_z]$ across the band was measured along a trajectory located close to the left edge of face 1, as indicated in Fig. 5c, via a ZYGO interferometer. The in-plane relative displacement jump across the band $[u_{xy}]$ was measured via an optical microscope, as shown in Fig. 5c.

For the narrow band 2, an AFM microscope, operated in contact mode, was used to measure the relative out-of-plane displacement profile $u_z(s)$ as a function of the distance s across the band (see Fig. 5c). For this band, it was assumed that the in-plane relative displacement u_{xy} was negligible: this was based on the observation that initially straight polishing marks in the proximity of the band remained straight after plastic deformation.

Analysis of strain profile in shear bands

The magnitude of the vector sum of the displacement jumps $[u_{xy}]$ and $[u_z]$ across a shear band, divided by the width of the band, gives the average shear strain in the band. For band 1, it was found that the shear strain was approximately 55% at 0.4% compressive plastic strain, and increased to 63% at a compressive plastic strain of 0.8%. In the case of band 2, the average shear strain was 3% at a compressive plastic strain of 0.4%, and it increased to approximately 6.5% when the overall compressive strain ε_c^{pl} in the cylindrical specimen reached 0.8%.

The detailed AFM measurements performed on band 2 (of width 15–30 μm) revealed that the plastic shear strain was not uniform across this small band. Figure 6 presents the AFM measurement of the out-of-plane displacement $u_z(s)$ as a function of the distance s across the band. This measurement, repeated at overall compressive plastic strains of 0.4 and 0.8%, allows for a calculation of the

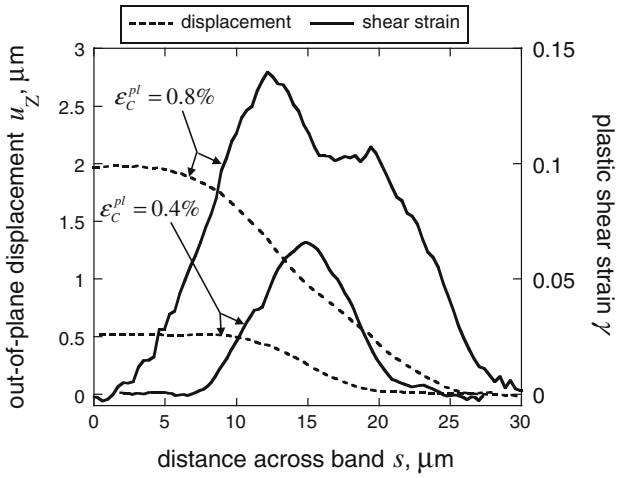

Fig. 6 Topology and plastic shear strain distribution in band 2, and their evolution with the imposed overall compressive plastic strain

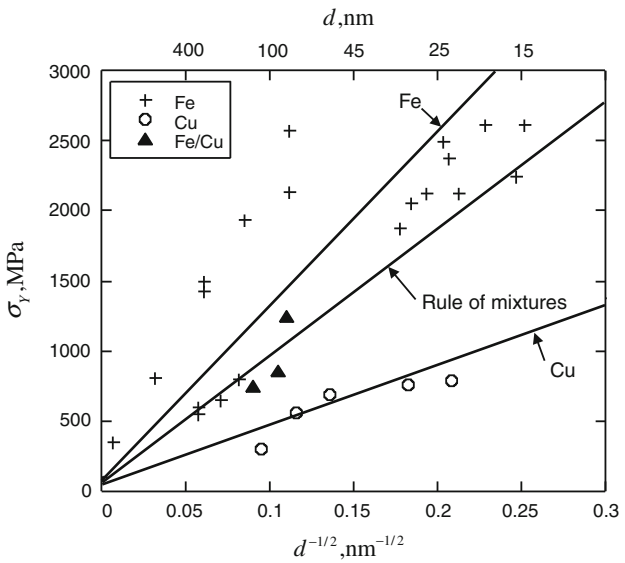

Fig. 7 The dependence of yield strength upon grain size for iron, copper and the iron/copper composites of this study

plastic shear strain in the band as $\gamma(s) = \mathrm{d}u_z/\mathrm{d}s$; the calculated $\gamma(s)$ is included in Fig. 6.

The shear strain displays a strong spatial gradient: $\gamma(s)$ is zero at the edges of the shear band and reaches a maximum in the centre. Figure 6 shows that both the maximum shear strain and the average shear strain, as well as the width of this shear band, all increase with the applied macroscopic compressive strain $\varepsilon_c^{\rho 1}$. For the larger band 1 (of width 50–100 μm), the low x–y resolution of the ZYGO interferometer did not allow for an accurate spatial measurement of the out-of-plane relative displacement profile $u_z(s)$. This profile was linear across the band, corresponding to a uniform shear strain, but detailed measurements of $u_z(s)$ and $\gamma(s)$ in the proximity of the edges of the band were not possible.

The optical images of the shear bands were processed to determine the volume fraction of the specimen occupied by shear bands. It was found that shear bands represent 8.8 and 12.2% of the specimen volumes at compressive plastic strains of 0.4 and 0.8%, respectively. These measurements can be used to estimate the average shear strain in the bands as a function of the overall imposed compressive plastic strain. Assuming that all bands are oriented at 45° on the specimen axis, the average shear strain is $\bar{\gamma} = 2\varepsilon_c^{\rho 1}/f$, where $\varepsilon_c^{\rho 1}$ is the overall compressive strain, and f is the volume fraction occupied by shear bands. It follows that $\bar{\gamma} = 9\%$ when $\varepsilon_c^{\rho 1} = 0.4\%$, and $\bar{\gamma} = 13\%$ when $\varepsilon_c^{\rho 1} = 0.8\%$.

Conclusions

The sources of strengthening

It will now be argued that the main source of strengthening is the small grain size of each phase. Additional strengthening is of less significance:

(i) solid solution strengthening within each phase, and
(ii) strengthening of the Fe phase by the pinning of dislocations by dissolved carbon.

Previous studies [14] have explored the dependence of strength of ferritic iron and of pure copper to grain size d. The measured yield strength σ_Y from these studies is plotted as a function of $d^{-1/2}$ in Fig. 7: a fit of these data by the Hall–Petch equation is included in the plot and accounts for the size effect in both copper and iron to within-material scatter. The data for Fe/Cu from this study have been added to the plot, along with the rule-of-mixtures line for the 60/40 Fe/Cu composite using the Hall–Petch fits. Note that this rule-of-mixtures line is a Voigt-type upper bound line assuming the same strain within the two phases. It is concluded that the upper yield strength of the Fe/Cu composites is due mainly to grain-boundary strengthening within each phase.

The strain distribution within a shear band

It is clear from Fig. 6 that the strain distribution within each shear band is not uniform spatially. With increasing macroscopic plastic straining, the shear band broadens and the level of plastic strain within the band intensifies. These measurements qualitatively support the predictions of strain gradient theories of plasticity: these theories predict a non-uniform shear strain varying continuously from zero at the band boundary to a maximum value on the mid-plane of the band.

Acknowledgements The authors are grateful for the support received from the European Union through the funding of the MANUDIRECT project (www.manudirect.eu).

References

1. Meyers MA, Mishra A, Benson DJ (2006) Prog Mater Sci 51:427
2. Suryanarayana C (1995) Int Mat Rev 40:41
3. Vajpai S, Dube R (2009) J Mater Sci 44(1):129. doi:10.1007/s10853-008-3111-2
4. Sanders PG, Eastman JA, Weertman JR (1997) Acta Mater 45:4019
5. Suryanarayana R, Frey CA, Sastry SML, Waller BE, Buhro WE (1996) In: Suryanarayana C, Singh J, Froes FH (eds) Processing and properties of nanocrystalline materials. TMS, Warrendale
6. Khan AS, Farrokh B, Takacs L (2008) J Mater Sci 43(9):3305. doi:10.1007/s10853-008-2508-2
7. Zhang X, Wang H, Scattergood RO, Narayan J, Koch CC (2002) Acta Mater 50:3995
8. Commentz B, Hartig C, Mecking H (1999) Comp Mater Sci 16:237
9. He L, Allard LF, Ma E (2000) Scripta Mater 42:517
10. He L, Ma E (1996) NanoStruc Mater 3(7):327
11. Carsley JE, Fisher A, Milligan WW, Aifantis EC (1998) Metall Mater Trans A 29A:2261
12. Cottrell AH, Bilby BA (1949) Proc Phys Soc (London) 62A:49
13. Fleck NA, Willis JW (2009) A mathematical basis for strain gradient plasticity theory. Part II: tensorial plastic multiplier. J Mech Phys Solids 57:1045–1057
14. Benson DJ, Fu H-H, Meyers MA (2001) Mater Sci Eng A319–321:854